Active Contact Forces Drive Non-Equilibrium Fluctuations in Membrane Vesicles Supplemental Material

Sho C. Takatori and Amaresh Sahu

1. EXPERIMENTAL METHODOLOGY

The main text contains a description of our experimental methods; in this section, we provide additional experimental details. Membrane fluctuations were measured by epifluorescence microscopy using a Nikon Eclipse Ti inverted microscope with a 60x/NA 1.4 Plan Apo objective. We recorded hundreds of consecutive images of the equatorial cross-section of a vesicle with a digital CCD camera, with an exposure time of 50 ms. An in-house code, based on Canny edge detection, was used to detect the edges of the membrane vesicle, and existing methods were applied to compute the transverse height fluctuations of giant unilamellar vesicles [1, 2].

The positions of the membrane edge are projected onto a Fourier series with 50 modes, according to

$$r(\theta,t) = R(t)\left(1 + \sum_{m=1}^{50} a_m \cos(m\theta) + b_m \sin(m\theta)\right), \tag{1}$$

where $R(t)$ is the vesicle radius at time t and m is the mode number. The height fluctuations of the membrane are given by

$$\left\langle \left|\hat{h}(k_x,t)\right|^2 \right\rangle = \frac{\pi R_0^3}{2}\left(\langle |c_m|^2\rangle - \langle |c_m|\rangle^2\right), \tag{2}$$

where $R_0 = \langle R(t)\rangle$ is the time-averaged vesicle radius, $k_x = m/R_0$ is the wave vector, and the Fourier coefficients $|c_m| = (a_m^2 + b_m^2)^{1/2}$. As only the transverse fluctuations along the equatorial cross-section of the vesicle are captured in the experiments, our data is implicitly averaged over longitudinal, out-of-focus fluctuations. Accordingly, we average our analytical theory over one of the two independent modes, such that our passive experimental results can be compared to equilibrium theory.

In practice, one long experimental acquisition was broken into 30 independent segments, and the fluctuations were computed for each segment. All experimental results in this work report a mean over these independent segments, with the relative error computed as $0.434 \times \sigma(\langle|\hat{h}|^2\rangle)/\chi(\langle|\hat{h}|^2\rangle$—where $\sigma(z)$ and $\chi(z)$ are the standard deviation and mean of a set of data z. We use the method described in Ref. [3] to report symmetric error bars on a logarithmic scale.

As noted in other studies [4, 5], fluctuations with a lifetime shorter than the integration time of the camera (i.e. aperture time of the camera shutter) are not correctly fitted. For the active vesicles, where fluctuation amplitudes are large and long lasting, we do not anticipate the finite camera integration time to influence our results.

1.1 Results

Here, we present experimental results, using the methodology described above to compute the Fourier transform of vesicle deformations as well as their fluctuation spectrum. Figure 1(a) shows an instantaneous snapshot of a vesicle with a protrusion caused by contact forces of a motile *B. subtilis* (top), and the corresponding radial profile of the vesicle edge about its center (bottom). Figure 1(b) is the probability distribution of membrane deflections experienced by the vesicle containing non-motile ('passive', in black symbols) and motile ('active', in red symbols) bacteria. Solid curves are Gaussian distributions, where the width ℓ is a function of membrane bending stiffness, tension, and the relevant driving force of the fluctuations. For passive vesicles, ℓ is governed by the thermal energy k_BT, whereas the active vesicles have a distribution governed by the activity scale $\zeta U_0^2 \tau_R$, where ζ is the hydrodynamic drag factor on the motile bacteria, U_0 is the swimming speed, and τ_R is the reorientation time of the bacteria. Because the activity scale $\zeta U_0^2 \tau_R \gg k_BT$, the active probability distribution is significantly wider than its passive counterpart, as shown in Fig. 1(b).

The aforementioned probability distributions demonstrate that when vesicles contain motile bacteria, the magnitude of membrane deformation increases. We infer further information about the membrane deflections by plotting the height fluctuation spectra, which are calculated according to Eqs. (1) and (2). Figure 2 shows the fluctuation spectrum

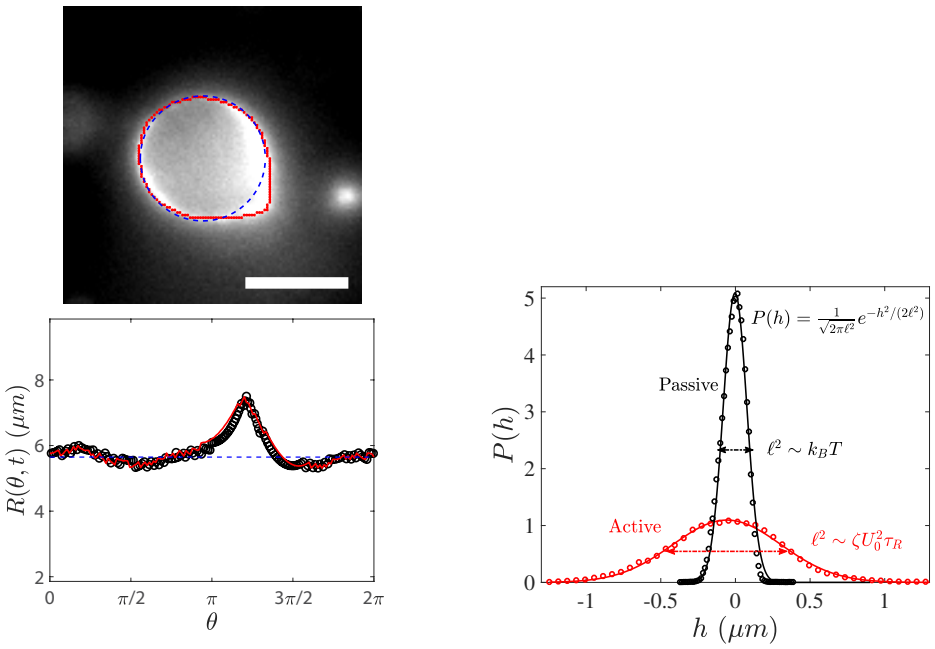

(a) Instantaneous snapshot of a giant unilamellar vesicle containing motile bacteria.

(b) Distribution of membrane deflections with and without active forces

FIG. 1. (a) Instantaneous fluorescence image of a giant unilamellar vesicle containing motile *B. subtilis* (not visible), and corresponding Fourier transform analysis. Above, blue dashed circle corresponds to the vesicle baseline position about its center, and the red dots indicate the location of the vesicle membrane edge. The scale bar is 10 μm. Below, black circles are the radial positions along the vesicle edge, and the red curve is the Fourier series to the data. (b) Normalized probability distribution of membrane deflections about the mean vesicle radius, for passive (black symbols) and active (red symbols) vesicles. The distribution was computed by binning over the angular positions around the vesicle and measuring the height deflection from the radial profile from (a). Solid curves are a fit to a Gaussian distribution, where ℓ is the width of the distribution.

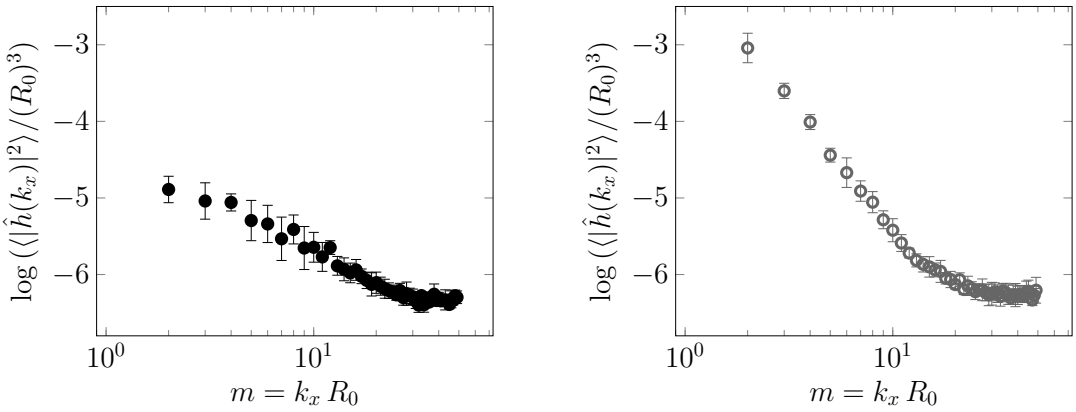

(a) Passive membrane.

(b) Active membrane.

FIG. 2. Membrane shape fluctuation spectra of giant unilammelar vesicles containing several non-motile (left) and motile (right) *B. subtilis* PY79. Height fluctuations $\left\langle\left|\hat{h}(k_x)\right|^2\right\rangle$ are nondimensionalized with the average vesicle radius R_0, and plotted as a function of the mode number $m = k_x R_0$. The data above are plotted together in Fig. 2 of the main text. Error bars are reported as described in Sec. 1, and include measurements from 30 independent time trajectories on the same vesicle.

for passive (a) and active (b) vesicles. Comparing the two cases, there is a significant increase in magnitude of the fluctuations, however only at low modes. In the subsequent sections, we derive a theory that elucidates the underlying physics of these active fluctuations.

2. THEORY AND SIMULATION OF PASSIVE MEMBRANES

In this section, we model lipid membrane vesicles in thermal equilibrium with the surrounding fluid, following well-established techniques [6, 7]. First, equilibrium statistical mechanics is used to determine the membrane fluctuation spectrum. As equilibrium methods cannot be used to study the active membrane system of interest, we next present a dynamical equation involving membrane–fluid interactions, which is shown to recover the same fluctuation spectrum. Finally, we describe our methodology to simulate lipid membrane dynamics, which again is amenable to the addition of active forces, and provide our numerical results. We note that none of the theoretical or computational results in this section are new. Rather, we present these results for clarity, prior to extending them to active systems in subsequent sections.

2.1. Equilibrium Theory

We begin by considering a fluctuating lipid membrane in thermal equilibrium at temperature T. The Hamiltonian $\mathcal{H}$ of such a system was determined in the seminal works of P. B. Canham [8], W. Helfrich [9], and E. A. Evans [10], and was found to be given by

$$\mathcal{H} = \int \left(2\kappa H^2 + \lambda\right) \mathrm{d}a \ . \tag{3}$$

In Eq. (3), κ is the elastic bending modulus, H is the mean curvature, λ is the surface tension, and the integral is over the membrane surface. The first term in the integral in Eq. (3) accounts for the energetic cost of membrane bending, while the second term describes the energetic cost of creating additional area.

While lipid membranes may in general undergo arbitrarily large deformations, the present study is limited to modeling the simpler case of nearly planar membranes undergoing only small out-of-plane deformations. To describe such a membrane, the membrane height $h(\boldsymbol{x}, t)$ is specified above every point $\boldsymbol{x} = (x, y)$ in the x–y plane (Fig. 3). The aforementioned surface description is called a Monge parametrization [11], and is commonly used in the description of nearly planar membrane systems. A membrane patch with periodic boundary conditions is considered, such that the region associated with one period lies above an $L \times L$ square in the x–y plane. For the case of small deformations,

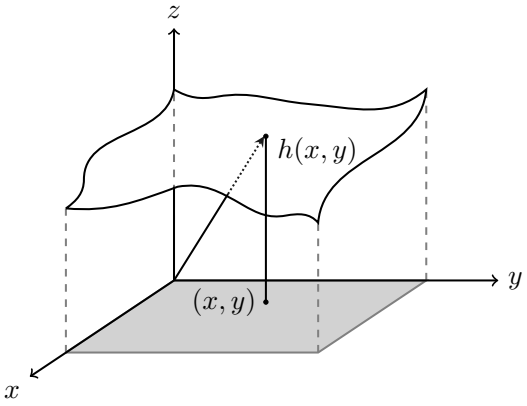

FIG. 3. A nearly planar lipid membrane patch. The membrane height $h(x, y)$ is specified above every point (x, y) in the x–y plane. The gray region depicts the $[0, L] \times [0, L]$ square over which the membrane is modeled, with periodic boundary conditions.

only terms up to second order in the height h are kept in the Hamiltonian (3), which simplifies to

$$\mathcal{H} = \frac{1}{2}\int \left(\kappa(\nabla^2 h)^2 + \lambda(\nabla h)^2\right) \mathrm{d}a \ . \tag{4}$$

As described in the main text, it is sometimes useful to describe lipid membrane fluctuations in Fourier space. To this end, the two-dimensional Fourier transform and inverse Fourier transform are respectively defined as

$$\hat{h}(\boldsymbol{k}, t) = \frac{1}{L}\int \mathrm{d}\boldsymbol{x}\ \mathrm{e}^{-i\boldsymbol{k}\cdot\boldsymbol{x}}\, h(\boldsymbol{x}, t) \tag{5}$$

and

$$h(\boldsymbol{x}, t) = \frac{1}{L}\sum_{\boldsymbol{k}} \hat{h}(\boldsymbol{k}, t)\, \mathrm{e}^{i\boldsymbol{k}\cdot\boldsymbol{x}} \ . \tag{6}$$

The inverse Fourier transform (6) sums only over discrete wave vectors $\boldsymbol{k}$ due to the periodic boundary condition requirement. By substituting Eq. (6) into Eq. (4), and assuming different bending modes are independent, one obtains

$$\mathcal{H} = \frac{1}{2}\sum_{\boldsymbol{k}} \left(\kappa k^4 + \lambda k^2\right) \left|\hat{h}(\boldsymbol{k})\right|^2 \ . \tag{7}$$

Applying the equipartition theorem to Eq. (7), the passive membrane fluctuation spectrum is found to be

$$\left\langle \left|\hat{h}(\boldsymbol{k})\right|^2 \right\rangle_{\mathrm{pas}} = \frac{k_{\mathrm{B}}T}{\kappa k^4 + \lambda k^2} \ . \tag{8}$$

To compare experimental measurements of lipid membrane fluctuations to theoretical results, we recognize experimental images are captured only at a single cross-section of the vesicle (see Fig. 1(a) in the main text). Thus, to compare with experimental results, the membrane fluctuation spectrum is averaged over all k_y modes according to

$$\left\langle \left|\hat{h}(k_x)\right|^2 \right\rangle := \frac{1}{2\pi}\int_{-\infty}^{\infty} \left\langle \left|\hat{h}(\boldsymbol{k}, t)\right|^2 \right\rangle \mathrm{d}k_y \ . \tag{9}$$

In the case of a passive vesicle in thermal equilibrium with the surrounding fluid, we substitute Eq. (8) into Eq. (9) to obtain

$$\left\langle \left|\hat{h}(k_x)\right|^2 \right\rangle_{\mathrm{pas}} = \frac{k_{\mathrm{B}}T}{2\lambda}\left(\frac{1}{k_x} - \frac{1}{\sqrt{k_x^2 + \lambda/\kappa}}\right) \ . \tag{10}$$

Equation (10) is used to compare theoretical and experimental results, and is plotted in Fig. 4 as well as Fig. 2 of the main text.

2.2. Non-Equilibrium Theory

The equilibrium results presented thus far rely on the equipartition theorem, which is not applicable in the presence of active forces. Consequently, in this section we describe a non-equilibrium theory which (i) models a lipid membrane sheet fluctuating in a Newtonian fluid, (ii) reproduces the membrane fluctuation spectrum (8), and (iii) is amenable to modeling active forces. We first describe the general continuum equation describing the lipid membrane shape, and then show how effects from the solvent are included. While the results of this section are well-known [6, 7], we introduce ideas such that they can be easily extended to the case of active membranes.

2.2.1. General Dynamical Equation of a Lipid Membrane

For a nearly planar membrane without a base flow, the linearized equation governing the membrane shape is given by

$$0 = [p] + \lambda\nabla^2 h - \kappa\nabla^4 h \ , \tag{11}$$

where $[p]$ is the jump in the normal traction across the membrane surface. The two other terms in Eq. (11) describe the internal membrane forces, arising from surface tension and bending effects, respectively, and have units of pressure. For notational convenience, we define the internal membrane force per area p^{int} as

$$p^{\text{int}} := \lambda\nabla^2 h - \kappa\nabla^4 h \ , \tag{12}$$

such that Eq. (11) can be written as $0 = [p] + p^{\text{int}}$.

2.2.2. Dynamical Equation with Surrounding Fluid

Thus far, we did not comment on the origin of the jump in the normal stress $[p]$ across the membrane surface (11). For the case of a passive membrane, $[p]$ captures the jump in the pressure of the surrounding bulk fluid. In particular, when a lipid membrane fluctuates in a fluid medium, it exerts forces on and experiences forces from the surrounding fluid. Consider a local shape change in the membrane: the membrane exerts some force on the fluid at that location, the force is transmitted through the fluid, and other regions of the membrane feel a resulting force. In this section, we first describe how a point force affects the surrounding fluid, and then obtain a dynamical equation which explicitly includes membrane–fluid interactions.

A Newtonian fluid with viscosity μ acted upon by a point force $\boldsymbol{f}\delta(\boldsymbol{r})$ at location $\boldsymbol{r} := (x, y, z) = \boldsymbol{0}$, with negligible inertia, is governed by the Stokes equations

$$\nabla \cdot \boldsymbol{v} = 0 \qquad \text{and} \qquad \mu\nabla^2\boldsymbol{v} - \nabla p + \boldsymbol{f}\delta(\boldsymbol{r}) = \boldsymbol{0} \ . \tag{13}$$

The Green's function solution of the pressure p and velocity $\boldsymbol{v}$ are well-known [12] to be given by

$$p(\boldsymbol{r}) = \frac{\boldsymbol{f}\cdot\boldsymbol{r}}{4\pi r^3} \qquad \text{and} \qquad \boldsymbol{v}(\boldsymbol{r}) = \boldsymbol{\Lambda}(\boldsymbol{r})\,\boldsymbol{f} \ , \tag{14}$$

where the Oseen tensor $\boldsymbol{\Lambda}(\boldsymbol{r})$ is defined as

$$\boldsymbol{\Lambda}(\boldsymbol{r}) := \frac{1}{8\pi\mu r}\left(\boldsymbol{I} - \frac{\boldsymbol{r}\otimes\boldsymbol{r}}{r^2}\right) . \tag{15}$$

Since the membrane deformations are assumed to be small, the forces on the fluid are primarily in the z-direction. Moreover, the resultant pressure and velocity fields at the membrane surface can be approximated by setting $z = 0$ in Eq. (14). For $\boldsymbol{f} = f\boldsymbol{e}_z$ and $z = 0$, the fluid pressure $p(x, y, z = 0) = f\delta(x)\delta(y)/4\pi$; the fluid velocity is given by

$$\boldsymbol{v}(x, y, z = 0) = \frac{f}{8\pi\mu\sqrt{x^2 + y^2}}\,\boldsymbol{e}_z \ . \tag{16}$$

We also define the $\boldsymbol{e}_z \otimes \boldsymbol{e}_z$ component of the Oseen tensor at $z = 0$ as

$$\Lambda(\boldsymbol{x}) := \frac{1}{8\pi\mu|\boldsymbol{x}|} \ , \tag{17}$$

where $\boldsymbol{x} = (x, y)$, such that Eq. (16) can be equivalently written as $\boldsymbol{v}(\boldsymbol{x}, 0) = \Lambda(\boldsymbol{x})\, f\boldsymbol{e}_z$.

For a nearly planar lipid membrane in contact with the surrounding fluid, a no-slip boundary condition between the membrane and the bulk fluid can be written as

$$\frac{\partial h}{\partial t}(\boldsymbol{x}, t) \ = \ v_z(\boldsymbol{x}, z = 0, t) \ + \ \eta(\boldsymbol{x}, t) \ , \tag{18}$$

where $\eta(\boldsymbol{x}, t)$ is a Gaussian random variable capturing perturbations from the surrounding fluid. Moreover, given a field of point forces per unit area $p(\boldsymbol{x}, z = 0, t)$ on the fluid, the z-component of the fluid velocity at $z = 0$ is given by

$$v_z(\boldsymbol{x}, z = 0, t) \ = \ \int \mathrm{d}\boldsymbol{x}'\, \Lambda(\boldsymbol{x} - \boldsymbol{x}')\ p(\boldsymbol{x}, z = 0, t) \ . \tag{19}$$

The field $p(\boldsymbol{x}, z = 0, t)$ in this case is known to be the force on the fluid by the membrane, which is equal and opposite to the force on the membrane by the fluid—the latter of which is $[p]$. Thus, according to Eq. (11),

$$p(\boldsymbol{x}, z = 0, t) = -[p] = p^{\text{int}} = \lambda\nabla^2 h - \kappa\nabla^4 h \ , \tag{20}$$

such that by combining Eqs. (18)–(20) we find the dynamical equation governing passive membrane fluctuations is given by [6, 13]

$$\frac{\partial h(\boldsymbol{x},t)}{\partial t} = \eta(\boldsymbol{x},t) + \int \mathrm{d}\boldsymbol{x}'\, \Lambda(\boldsymbol{x}-\boldsymbol{x}')\, p^{\mathrm{int}}(\boldsymbol{x}',t) \ . \tag{21}$$

When characterizing the thermal forces on the membrane from the fluid, as well as when simulating membrane height fluctuations, it is most convenient to work in Fourier space, where the height modes decouple. To take the Fourier transform of Eq. (21), we first provide the well-known convolution theorem. For a general function $f(\boldsymbol{x},t)$, we have

$$\begin{aligned}\int \mathrm{d}\boldsymbol{x}'\, \Lambda(\boldsymbol{x}-\boldsymbol{x}')\, f(\boldsymbol{x}',t) &= \int \mathrm{d}\boldsymbol{x}'\, \frac{1}{L}\sum_{\boldsymbol{k}} \hat{\Lambda}(\boldsymbol{k}) \mathrm{e}^{i\boldsymbol{k}\cdot(\boldsymbol{x}-\boldsymbol{x}')}\, f(\boldsymbol{x}',t) \\ &= \sum_{\boldsymbol{k}} \hat{\Lambda}(\boldsymbol{k})\, \mathrm{e}^{i\boldsymbol{k}\cdot\boldsymbol{x}}\, \frac{1}{L}\int \mathrm{d}\boldsymbol{x}'\, f(\boldsymbol{x}',t)\, \mathrm{e}^{-i\boldsymbol{k}\cdot\boldsymbol{x}'} \\ &= \sum_{\boldsymbol{k}} \hat{\Lambda}(\boldsymbol{k})\, \hat{f}(\boldsymbol{k},t)\, \mathrm{e}^{i\boldsymbol{k}\cdot\boldsymbol{x}} \ ,\end{aligned} \tag{22}$$

where in the first line we substituted the Fourier transform of $\Lambda(\boldsymbol{x}-\boldsymbol{x}')$, in the second line we rearranged terms, and in the third line we recognized the form of $\hat{f}(\boldsymbol{k},t)$. With the result of Eq. (22) and the Fourier transform definitions (5, 6), Eq. (21) can be written as

$$\frac{\partial}{\partial t}\left(\frac{1}{L}\sum_{\boldsymbol{k}} \hat{h}(\boldsymbol{k},t)\, \mathrm{e}^{i\boldsymbol{k}\cdot\boldsymbol{x}}\right) = \frac{1}{L}\sum_{\boldsymbol{k}} \hat{\eta}(\boldsymbol{k},t)\, \mathrm{e}^{i\boldsymbol{k}\cdot\boldsymbol{x}} + \sum_{\boldsymbol{k}} \hat{\Lambda}(\boldsymbol{k})\, \hat{p}^{\mathrm{int}}(\boldsymbol{k},t)\, \mathrm{e}^{i\boldsymbol{k}\cdot\boldsymbol{x}} \ , \tag{23}$$

which implies

$$\frac{\partial \hat{h}(\boldsymbol{k},t)}{\partial t} = L\hat{\Lambda}(\boldsymbol{k})\, \hat{p}^{\mathrm{int}}(\boldsymbol{k},t) + \hat{\eta}(\boldsymbol{k},t) \ . \tag{24}$$

The quantities $\hat{\Lambda}(\boldsymbol{k})$ and $\hat{p}^{\mathrm{int}}(\boldsymbol{k},t)$ are calculated as

$$\hat{\Lambda}(\boldsymbol{k}) = \frac{1}{4\mu k L} \qquad \text{and} \qquad \hat{p}^{\mathrm{int}}(\boldsymbol{k},t) = -\left(\lambda k^2 + \kappa k^4\right) \hat{h}(\boldsymbol{k},t) \ , \tag{25}$$

such that Eq. (24) can be written as

$$\frac{\partial \hat{h}(\boldsymbol{k},t)}{\partial t} = -\omega(k)\, \hat{h}(\boldsymbol{k},t) + \hat{\eta}(\boldsymbol{k},t) \ , \tag{26}$$

where the relaxation frequency $\omega(k)$ is given by

$$\omega(k) = \frac{1}{4\mu}\left(\lambda k + \kappa k^3\right) \ . \tag{27}$$

In Eq. (26), the Fourier transform of the thermal noise, $\hat{\eta}(\boldsymbol{k},t)$, satisfies the fluctuation–dissipation theorem, such that

$$\left\langle \hat{\eta}(\boldsymbol{k},t) \right\rangle = 0 \ , \tag{28}$$

$$\left\langle \mathrm{Re}\{\hat{\eta}(\boldsymbol{k},t)\}\, \mathrm{Im}\{\hat{\eta}(\boldsymbol{k}',t')\} \right\rangle = 0 \ , \tag{29}$$

$$\left\langle \mathrm{Re}\{\hat{\eta}(\boldsymbol{k},t)\}\, \mathrm{Re}\{\hat{\eta}(\boldsymbol{k}',t')\} \right\rangle = k_{\mathrm{B}} T L\, \hat{\Lambda}(\boldsymbol{k})\, \delta(t-t') \left(\delta_{\boldsymbol{k},\boldsymbol{k}'} + \delta_{\boldsymbol{k},-\boldsymbol{k}'}\right) \ , \tag{30}$$

and

$$\left\langle \mathrm{Im}\{\hat{\eta}(\boldsymbol{k},t)\}\, \mathrm{Im}\{\hat{\eta}(\boldsymbol{k}',t')\} \right\rangle = k_{\mathrm{B}} T L\, \hat{\Lambda}(\boldsymbol{k})\, \delta(t-t') \left(\delta_{\boldsymbol{k},\boldsymbol{k}'} - \delta_{\boldsymbol{k},-\boldsymbol{k}'}\right) \ . \tag{31}$$

2.3. Simulation Methodology

In this section, we closely follow the simulation procedure detailed in Ref. [6]. Due to the decoupling of the height modes in Fourier space, each mode is simulated independently. For a membrane over an $L \times L$ patch with periodic boundary conditions, the allowed wave vectors are

$$\boldsymbol{k} = (m, n)\,\frac{2\pi}{L}\,, \qquad m, n \in \mathbb{Z}\,. \tag{32}$$

A space of linearly independent wave numbers, $\mathcal{Q}$, is defined as

$$\mathcal{Q} = \big\{(1 \le m \le M, n = 0) \cup (0 \le m \le M, 1 \le n \le M)\big\}\,, \tag{33}$$

where M defines the largest wave vector considered. The mode $\boldsymbol{k} = \boldsymbol{0}$ is ignored, as it describes only rigid translations of the membrane patch.

To simulate the time evolution of the membrane height modes, Eq. (26) is integrated from time t to $t + \Delta t$ to yield

$$\int_t^{t+\Delta t} \mathrm{d}t'\; \frac{\partial \hat{h}(\boldsymbol{k}, t')}{\partial t'} \;=\; -\omega(k) \int_t^{t+\Delta t} \mathrm{d}t'\; \hat{h}(\boldsymbol{k}, t') \;+\; \int_t^{t+\Delta t} \mathrm{d}t'\; \hat{\eta}(\boldsymbol{k}, t')\,. \tag{34}$$

Assuming Δt is small, the integrand of the first term on the right-hand side of Eq. (34) is moved outside the integral. Defining

$$\hat{R}(\boldsymbol{k}, t; \Delta t) := \int_t^{t+\Delta t} \mathrm{d}t'\; \hat{\eta}(\boldsymbol{k}, t')\,, \tag{35}$$

Eq. (34) can be written as

$$\hat{h}(\boldsymbol{k}, t + \Delta t) = \big(1 - \omega(k)\Delta t\big)\hat{h}(\boldsymbol{k}, t) + \hat{R}(\boldsymbol{k}, t; \Delta t)\,. \tag{36}$$

The complex Gaussian random noise $\hat{R}(\boldsymbol{k}, t; \Delta t)$ has mean zero and variance given by

$$\begin{aligned}
\big\langle \hat{R}(\boldsymbol{k}, t; \Delta t)\, \hat{R}^*(\boldsymbol{k}, t; \Delta t) \big\rangle &= \int_t^{t+\Delta t} \mathrm{d}t' \int_t^{t+\Delta t} \mathrm{d}t''\; \big\langle \hat{\eta}(\boldsymbol{k}, t') \hat{\eta}^*(\boldsymbol{k}, t'') \big\rangle \\
&= \int_t^{t+\Delta t} \mathrm{d}t' \int_t^{t+\Delta t} \mathrm{d}t'' \left(\Big\langle \mathrm{Re}\{\hat{\eta}(\boldsymbol{k}, t')\}\, \mathrm{Re}\{\hat{\eta}(\boldsymbol{k}, t'')\} \Big\rangle \right. \\
&\qquad \left. + \Big\langle \mathrm{Im}\{\hat{\eta}(\boldsymbol{k}, t')\}\, \mathrm{Im}\{\hat{\eta}(\boldsymbol{k}, t'')\} \Big\rangle \right) \\
&= 2 k_{\mathrm{B}} T L \hat{\Lambda}(\boldsymbol{k}) \Delta t\,,
\end{aligned} \tag{37}$$

where in the first equality Eq. (35) was substituted, in the second equality $\hat{\eta}$ was split into real and imaginary parts and Eq. (29) was used to eliminate cross terms, and in the third equality Eqs. (30) and (31) were substituted. Defining r_1 and r_2 to be independent, normally distributed random numbers, the height modes are evolved numerically according to

$$\hat{h}(\boldsymbol{k}, t + \Delta t) = \big(1 - \omega(k)\Delta t\big)\hat{h}(\boldsymbol{k}, t) + \big(r_1 + i\, r_2\big)\sqrt{k_{\mathrm{B}} T L \hat{\Lambda}(\boldsymbol{k}) \Delta t}\,. \tag{38}$$

Note that in Eq. (38), r_1 and r_2 are used to distribute the random noise in both the real and imaginary directions, each with a variance of one-half the result of Eq. (37). In practice, the real and imaginary components of the height modes are simulated independently. Our code to calculate the fluctuation spectrum by evolving height modes according to Eq. (38) is provided at https://github.com/mandadapu-group/active-contact.

2.4. Theoretical, Numerical, and Experimental Results

We now present the results of passive numerical simulations to (i) show the numerical scheme reproduces equilibrium fluctuations, and (ii) demonstrate how simulations are compared to experiments. For each wave vector $\boldsymbol{k}$, the

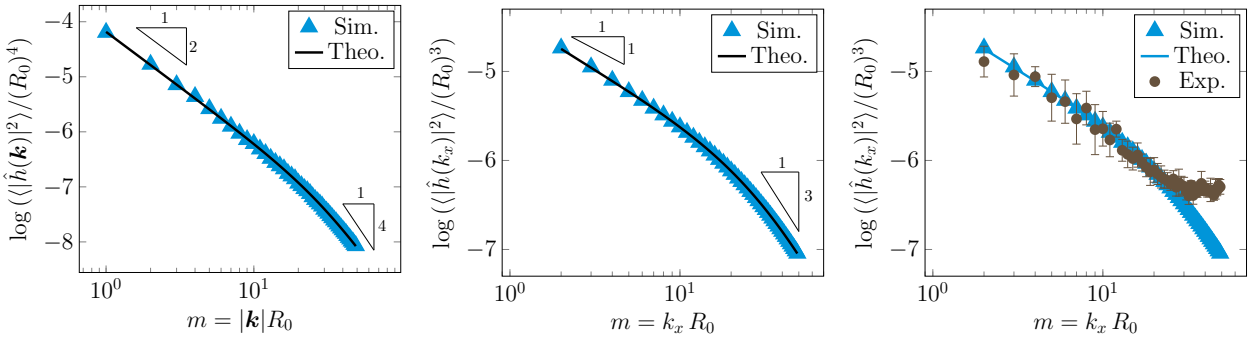

(a) passive, no average (b) passive, average (c) passive, average, with data

FIG. 4. Passive thermal fluctuations of a lipid membrane in thermal equilibrium with the surrounding fluid. (a) Comparison of dynamical simulations, as described in Sec. 2.3 (blue triangles) and the known equilibrium result of Eq. 8 (black curve). The quantitative agreement indicates the code is working as expected. (b) The result of averaging the simulation result and theoretical prediction over k_y modes, according to Eq. (39). (c) Experimental passive data overlaid on the averaged passive result. The systematic discrepancy at large k_x occurs due to the pixel resolution of the camera. In all simulations and presented theoretical results, parameters are $\lambda = 4 \cdot 10^{-3}$ pN/nm, $\kappa = 14.3\, k_{\mathrm{B}}T$ at $T = 30°\mathrm{C}$, $R_0 = 4\,\mu$m, $\mu = 0.7972$ mPa·s, and height fluctuations were simulated over 0.7 s.

simulations generate $\mathrm{Re}\{\hat{h}(\boldsymbol{k},t)\}$ and $\mathrm{Im}\{\hat{h}(\boldsymbol{k},t)\}$ over time, with which $\left\langle\left|\hat{h}(\boldsymbol{k},t)\right|^2\right\rangle_{\mathrm{pas}}$ is calculated. As shown in Fig. 4(a), the simulations (blue triangles) exactly match the known theoretical result (Eq. (8), black line).

As vesicles are imaged experimentally at a single cross-section, all Fourier modes orthogonal to this cross-section are implicitly summed over. To compare simulation results with experiments, the height fluctuations of the nearly planar membrane are averaged over k_y modes according to Eq. (9). In practice, the averaging is done numerically, according to

$$\left\langle\left|\hat{h}(k_x,t)\right|^2\right\rangle = \frac{2}{L}\sum_{n=0}^{M}\left\langle\left|\hat{h}\big(\boldsymbol{k}=(k_x,2\pi n/L),t\big)\right|^2\right\rangle . \tag{39}$$

Moreover, the length L in simulations is set to $L = 2\pi R_0$, where R_0 is the radius of the undeformed membrane vesicle, to be consistent with the Fourier transform of experimental data (see Eq. (1)). In averaging our simulation results according to Eq. (39), we obtain the results shown as blue triangles in Fig. 4(b), which agree with the theoretical calculation of Eq. (10) (black line). In Fig. 4(c), the data contained in Fig. 4(b) are overlaid with experimental data. Figure 4(c) contains the same information as the passive portion of Fig. 2 in the main text, following the same color scheme.

3. THEORY AND SIMULATION OF ACTIVE MEMBRANES

In this section, the non-equilibrium theory and simulations of Sec. 2 are extended to model lipid membrane vesicles acted upon by active bacterial contact forces. When bacteria push on the membrane surface, a new force enters the membrane shape equation, which in turn is transmitted throughout the fluid to exert forces at other locations on the membrane surface. Importantly, we spread the bacterial contact force over the width of a bacterium, and recognize the characteristic duration of bacterial–membrane contact is much larger than the timescale of membrane fluctuations, $1/\omega(q)$. As a result, the membrane fluctuation spectrum can be written as the sum of two terms: an equilibrium term identical to that of a passive membrane, and an active term involving details of the bacterial contact force.

3.1. Non-Equilibrium Contact Theory

With a model for the dynamical height fluctuations of a passive membrane vesicle, we now seek to describe the active membrane fluctuations resulting from self-propelled bacteria contained within a membrane vesicle. The active

particles exert a force on the membrane, which we approximate by the active force per area

$$p^{\mathrm{act}} = \sum_{j=1}^{N_{\mathrm{c}}} \bar{p}\,\phi(t;t_j)\,\exp\left\{-\frac{(\boldsymbol{x}-\boldsymbol{x}_j)^2}{2a^2}\right\}. \tag{40}$$

In Eq. (40), N_{c} is the number of collision events, with the j^{th} active particle–membrane collision occurring at time t_j and position $\boldsymbol{x}_j$. The only dimensional quantity on the right-hand side of Eq. (40) is $\bar{p}$, which captures the maximum pressure exerted by the particle on the membrane. As a simple approximation, we set $\bar{p} = 2\lambda/a$, where a is the half-width of a bacterium and $\bar{p}$ would be the pressure exerted by a membrane on a sphere of radius a. The Gaussian contribution in Eq. (40) describes the spreading of the particle–membrane contact point force over an area. Lastly, $\phi(t;t_j)$ approximates the temporal nature of the particle–membrane collision. As shown in Fig. 3b in the main text, $\phi(t;t_j)$ is an isosceles trapezoid centered at time t_j with top length τ_{R} and bottom length $\tau_{\mathrm{R}} + 2\tau_{\mathrm{P}}$; $\tau_{\mathrm{P}} \approx 0.05$ sec is an estimate of how long it takes for a bacterium to come to a complete stop due to elastic membrane forces, once it makes initial contact with the membrane.

With a characterization of the active forces on the membrane, we follow an identical procedure to that of the passive case. The jump in the normal traction acting on the membrane is now given by $[p] = -p^{\mathrm{tot}} + p^{\mathrm{act}}$, such that the magnitude of the total force per area p^{tot} acting on the membrane by the surrounding fluid can be written as

$$p^{\mathrm{tot}}(\boldsymbol{x},t) = p^{\mathrm{int}}(\boldsymbol{x},t) + p^{\mathrm{act}}(\boldsymbol{x},t)\,. \tag{41}$$

Recognizing $p(\boldsymbol{x}, z=0, t) = p^{\mathrm{tot}}$ (c.f. Eqs. (19) and (20)), we find the active analog of Eq. (21) is given by

$$\frac{\partial h(\boldsymbol{x},t)}{\partial t} = \eta(\boldsymbol{x},t) + \int \mathrm{d}\boldsymbol{x}'\,\Lambda(\boldsymbol{x}-\boldsymbol{x}')\left[p^{\mathrm{int}}(\boldsymbol{x}',t) + p^{\mathrm{act}}(\boldsymbol{x}',t)\right]. \tag{42}$$

Again taking the Fourier transform of Eq. (42) and using the convolution theorem (22), we obtain

$$\frac{\partial \hat{h}(\boldsymbol{k},t)}{\partial t} = -\omega(k)\,\hat{h}(\boldsymbol{k},t) + \hat{\eta}(\boldsymbol{k},t) + L\hat{\Lambda}(\boldsymbol{k})\,\hat{p}^{\mathrm{act}}(\boldsymbol{k},t)\,, \tag{43}$$

where the Fourier transform of the active pressure is calculated to be

$$\hat{p}^{\mathrm{act}}(\boldsymbol{k},t) = \sum_{j=1}^{N_{\mathrm{c}}} \frac{a^2\,\bar{p}}{R_0}\,\phi(t;t_j)\,\exp\left\{-i\boldsymbol{x}_j\cdot\boldsymbol{k} - \frac{a^2\,k^2}{2}\right\}. \tag{44}$$

In Eq. (44), we substituted $L = 2\pi R_0$ to simplify the expression. By substituting Eqs. $(25)_1$ and (44) into Eq. (43), we obtain

$$\frac{\partial \hat{h}(\boldsymbol{k},t)}{\partial t} = -\omega(k)\,\hat{h}(\boldsymbol{k},t) + \hat{\eta}(\boldsymbol{k},t) + \sum_{j=1}^{N_{\mathrm{c}}} \frac{a^2\,\bar{p}}{4\mu k R_0}\,\phi(t;t_j)\,\exp\left\{-i\boldsymbol{x}_j\cdot\boldsymbol{k} - \frac{a^2\,k^2}{2}\right\}. \tag{45}$$

Equation (45) is presented as Eqs. (3) and (4) in the main text. As discussed in the main text, an approximate solution of the height fluctuation spectrum given by Eq. (45) is found to be

$$\langle|\hat{h}(\boldsymbol{k})|^2\rangle = \frac{k_{\mathrm{B}}T}{\kappa k^4 + \lambda k^2} + \frac{N_{\mathrm{p}}\,\tau_{\mathrm{R}}}{\tau_{\mathrm{T}} + \tau_{\mathrm{R}}}\left(\frac{a^2\,\bar{p}/R_0}{\kappa k^4 + \lambda k^2}\right)^2 \mathrm{e}^{-a^2k^2}\,, \tag{46}$$

where N_{p} is the number of enclosed bacteria, τ_{R} is the bacteria reorientation time, and τ_{T} is the time it takes the bacteria to travel from one side of the vesicle to the other.

3.2. Simulation Methodology

Just as the active non-equilibrium theory is an extension of its passive analog, we extend the passive simulation methodology to simulate lipid membrane vesicles being acted upon by active contact forces. By integrating Eq. (45)

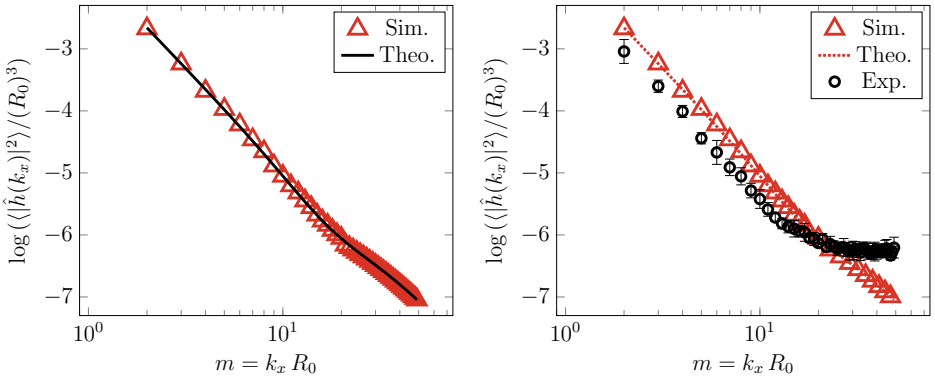

(a) active, average (b) active, average, with data

FIG. 5. Active lipid membrane fluctuations. (a) Simulation results (red triangles) show excellent agreement with the theoretical prediction (black curve, expression in main text). (b) Experimental data overlaid on the same plot. Again, the system leveling off of the experimental fluctuations at large k_x occurs due to camera resolution and the intrinsic noise present at large wave vectors. All simulation parameters are identical to those detailed in Fig. 4, and additional details can be found in our code—provided at https://github.com/mandadapu-group/active-contact.

from time t to $t + \Delta t$ and recognizing only the active pressure term is new, we find the height modes are evolved according to

$$\hat{h}(\boldsymbol{k}, t+\Delta t) = \big(1 - \omega(k)\Delta t\big)\hat{h}(\boldsymbol{k}, t) + \big(r_1 + i\, r_2\big)\sqrt{k_{\mathrm{B}} T L \hat{\Lambda}(\boldsymbol{k})\Delta t} + \sum_{j=1}^{N_{\mathrm{c}}} \frac{a^2\, \bar{p}\, \Delta t}{4\mu k R_0}\, \phi(t; t_j)\, \exp\left\{ - i\boldsymbol{x}_j \cdot \boldsymbol{k} - \frac{a^2\, k^2}{2} \right\}. \tag{47}$$

As before, the real and imaginary components of each membrane mode is simulated independently. In code, the number of collisions $N_{\mathrm{c}} = N_{\mathrm{p}} \cdot t_{\mathrm{sim}}/(\tau_{\mathrm{R}} + \tau_{\mathrm{T}})$, where $N_{\mathrm{p}} = 7$ is the number of particles, $t_{\mathrm{sim}} = 7$ sec is the total simulation time, $\tau_{\mathrm{R}} = 0.5$ sec is the bacterial reorientation time, and $\tau_{\mathrm{T}} = 0.5$ sec is the traversal time—the latter of which is the time it takes for the bacteria to go from one end of the vesicle to another, given the bacterial swim speed $U_0 \approx 15\,\mu$m/s. Moreover, the collision times t_j and position $\boldsymbol{x}_j$ are chosen randomly from a uniform distribution of times in the range $[0, t_{\mathrm{sim}}]$ and positions in the range $[0, L] \times [0, L]$, respectively. Again, our code is provided at https://github.com/mandadapu-group/active-contact.

3.3. Results

As shown in Fig. 5(a), there is excellent agreement between our simulation results and the theoretical prediction of Eq. (46). Note that Fig. 5 contains the same data as was presented in the main text, for which $N_{\mathrm{p}} \approx 7$ and $R_0 \approx 4$ μm. To test the robustness of our theoretical model, we now also provide an analysis of two additional active vesicles, as shown in Fig. 6: one with $N_{\mathrm{p}} \approx 10$ and $R_0 \approx 8$ μm, and another with $N_{\mathrm{p}} \approx 20$ and $R_0 \approx 15$ μm. In these experiments, the passive data was not available, and so the surface tension and bending modulus for these vesicles could not be obtained. In our analysis, we used the values of λ and κ from the 7-particle case. However, as we show in the following section, our theoretical results are insensitive to the values of λ and κ, and so we still obtain reasonable predictions given this limitation.

As seen in Fig. 6(a), the 10-particle vesicle again shows excellent agreement between experiments, simulation, and theory, thus demonstrating the validity of our numerical and analytical developments. The results from the 20-particle vesicle, on the other hand, suggest where our theory begins to break down. As shown in Fig. 6(b), although there is generally good agreement with the experimental data, there is a slight difference in the shape of the latter: active fluctuations at lower modes are slightly suppressed, while active fluctuations at intermediate modes are slightly enhanced. We believe this qualitative change is due to there being more bacteria enclosed within the vesicle. As can be seen from Figs. 6(c)–6(e), there are now often times where multiple bacteria contact a local portion of the membrane in quick succession. Due to their persistent motion, active particles have a tendency to accumulate at surfaces [14, 15],

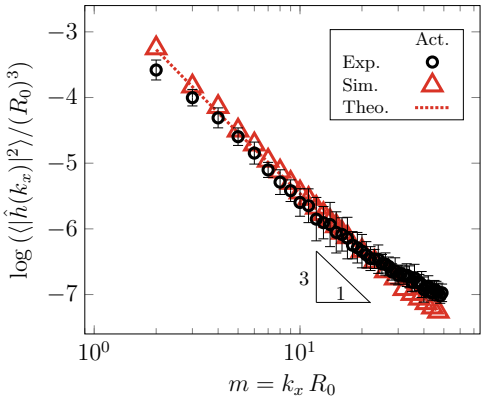

(a) Active fluctuations: $R_0 \approx 8$ μm, $N_\mathrm{p} \approx 10$

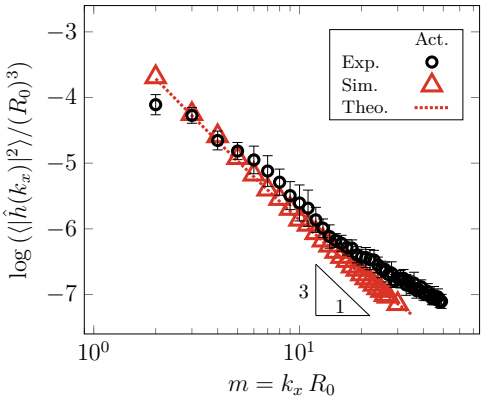

(b) Active fluctuations: $R_0 \approx 15$ μm, $N_\mathrm{p} \approx 20$

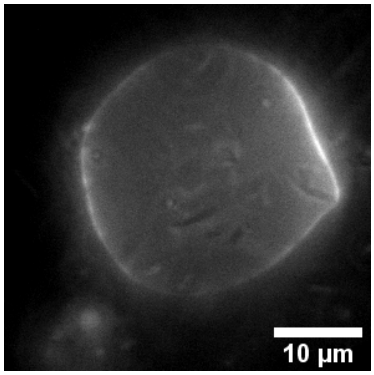

(c) Snapshot of a GUV (radius ≈ 15 μm) containing ≈ 20 motile bacteria, which are visible as black objects in the brightfield image.

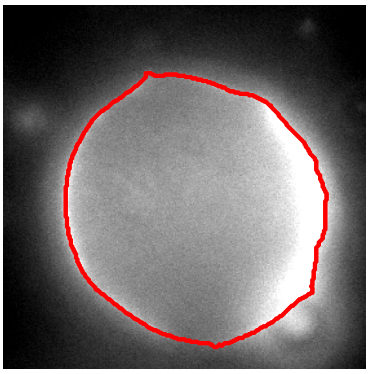

(d) Fluorescence image of the same GUV at a different time, which is used for height fluctuation analysis.

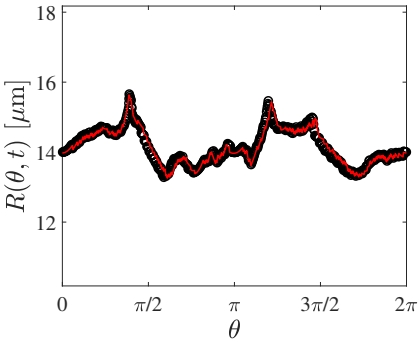

(e) Deformation of the membrane as a function of angle around the GUV.

FIG. 6. Experimental data for shape fluctuations of bacteria-containing vesicles, in two cases: (a) GUV with radius $R_0 \approx 8$ μm and $N_\mathrm{p} \approx 10$ bacteria, and (b) GUV with radius $R_0 \approx 15$ μm containing $N_\mathrm{p} \approx 20$ bacteria. (c)–(d) Instantaneous snapshots of the vesicle corresponding to case (b), via brightfield and fluorescence imaging. In (d), the red curve denotes the membrane contour, calculated using an edge-detection algorithm. (e) Membrane deformation as a function of arclength around the membrane perimeter. Black symbols are data and the red curve is the Fourier spectra to obtain the height fluctuations.

and it seems that in the 20-particle vesicle such effects are no longer negligible. Importantly, when multiple bacteria contact nearby regions of the membrane in rapid succession, large wavelength modes are effectively converted into shorter wavelength ones, as can be seen by comparing Fig. 1(a) with Fig. 6(e). In the former, the membrane receives isolated, single perturbations that relax fully before the membrane receives the next active perturbation, while in the latter, there is a superposition of many active perturbations which occur simultaneously—effectively decreasing the magnitude of low modes and increases the magnitude of intermediate ones. We thus find that while our theory captures the shape fluctuations of active membranes a cross a range of vesicle sizes and active particle numbers, it is most accurate when particle numbers are low and bacteria–bacteria correlations do not significantly affect bacteria–membrane interactions.

3.4 Parameter sensitivity analysis of theoretical model

In considering the experimental system, there are seven fundamental parameters: the bending modulus κ, surface tension λ, vesicle radius R_0, number of bacteria N_p, bacterial reorientation time τ_R, bacterial half-width a, and bacterial velocity U_0. From these, we approximate the magnitude of the contact pressure as $\bar{p} \approx 2\lambda/a$ and the bacterial traversal time $\tau_\mathrm{T} \approx 2R_0/U_0$. We have already experimentally demonstrated how changes to N_p and R_0 alter the active fluctuation spectrum, however the remaining parameters are not easily modified experimentally. Thus, we

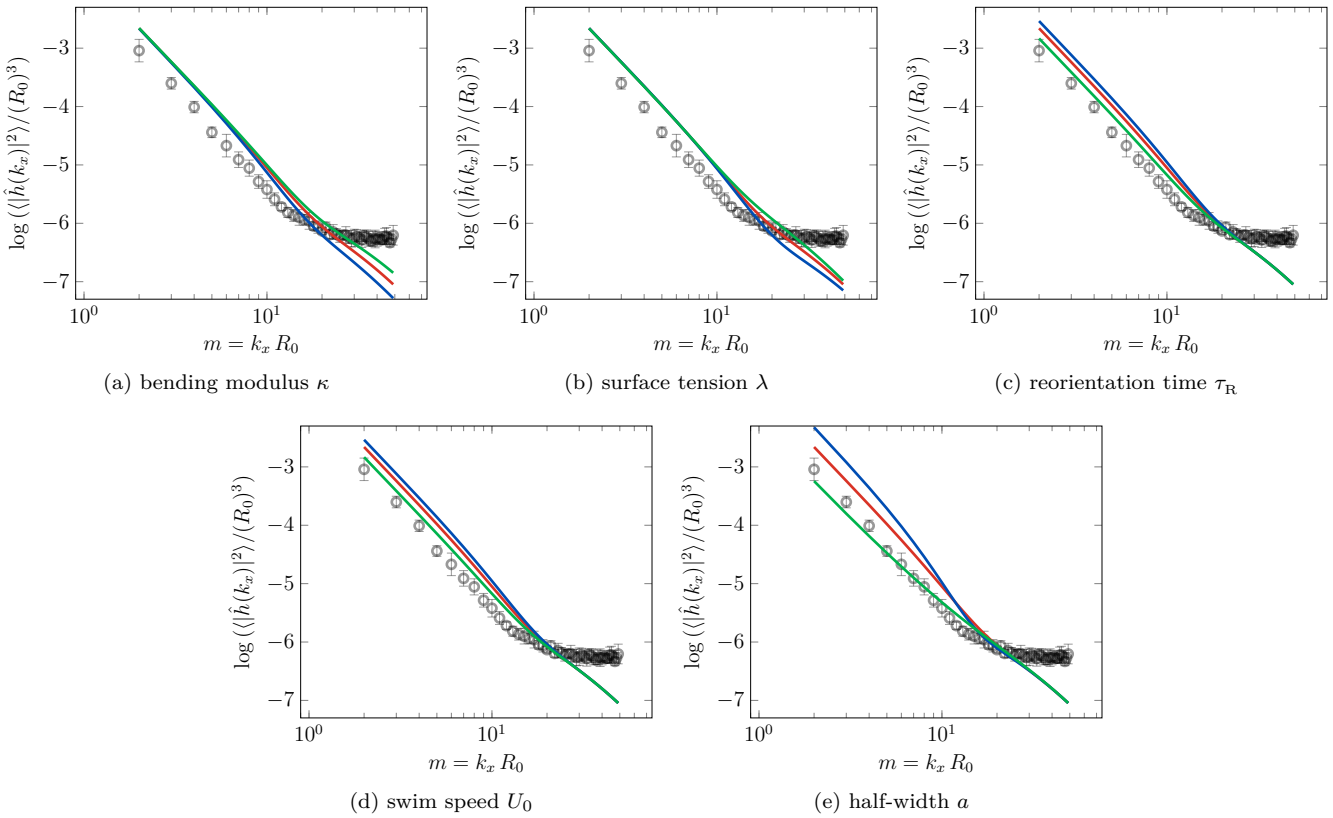

(a) bending modulus κ (b) surface tension λ (c) reorientation time τ_{R}

(d) swim speed U_0 (e) half-width a

FIG. 7. Sensitivity analysis of the theoretical result, Eq. (46), to changes in parameter values. In all cases, the red line is the theoretical result presented in Fig. 2 of the main text, and the open circles are the active fluctuation data. For plots (a)–(d), the green line represents a decrease in the chosen parameter by a factor of two, while the blue line represents an increase in the chosen parameter by a factor of two. For plot (e), as the analytical expression is sensitive to the bacterial half-width through the exponential term, the green line represents a decrease in the bacterial half-width by 50%, while the blue line represents an increase in the bacterial half-width by 50%.

understand how our theoretical results would change due to variations in the remaining fundamental parameters via a sensitivity analysis. As shown in Fig. 7, our analytical prediction is relatively sensitive to changes in the bacterial half-width a, but otherwise fairly insensitive to changes in the remaining parameters.

4. SUPPLEMENTAL VIDEOS

Below, we describe the Supplemental Videos associated with this manuscript. In all movies, the time stamp corresponds to minutes:seconds.

S1. Fluorescence movie of a giant unilamellar vesicle (GUV) containing several non-motile *B. subtilis*.

S2. Brightfield movie of a GUV containing several motile *B. subtilis*. The vesicle edges can be seen as a thin black line.

S3. Fluorescence movie of the same GUV as in Vid. S2, containing several motile *B. subtilis*. Bacteria are non-fluorescent and are not visible in this movie.

S4. Merged fluorescence and brightfield movie of the same GUV containing several motile *B. subtilis*.

S5. Merged fluorescence and brightfield movie of a floppy GUV containing motile *B. subtilis*. Membrane deformations are larger for this GUV.

S6. Merged fluorescence and brightfield movie of a GUV containing Janus particles in the absence of hydrogen peroxide. The scale bar is 10 μm.

S7. Merged fluorescence and brightfield movie of a GUV containing Janus particles in the presence of 0.5% hydrogen peroxide. Self propulsion of the Janus particles can be observed and their collisions with the membrane.

S8. Merged fluorescence and brightfield movie of a GUV containing many motile *B. subtilis*. Deformations are very large and thin membrane tubes can be seen. Each membrane tube contain a few bacteria that collided into the membrane.

[1] J. Pécréaux, H.-G. Döbereiner, J. Prost, J.-F. Joanny, and P. Bassereau, Eur. Phys. J. E **13**, 277 (2004).
[2] F.-C. Tsai, B. Stuhrmann, and G. H. Koenderink, Langmuir **27**, 10061 (2011).
[3] D. Baird, *Experimentation: An Introduction to Measurement Theory and Experiment Design* (Benjamin Cummings, 3rd Ed., 1994).
[4] P. Méléard, J. Faucon, M. Mitov, and P. Bothorel, Europhys. Lett. **19**, 267 (1992).
[5] P. Méléard, T. Pott, H. Bouvrais, and J. H. Ipsen, Eur. Phys. J. E **34**, 116 (2011).
[6] K. Sapp and L. Maibaum, Phys. Rev. E **94**, 052414 (2016).
[7] L. C.-L. Lin and F. L. H. Brown, Phys. Rev. Lett. **93**, 256001 (2004).
[8] P. B. Canham, J. Theor. Biol. **26**, 61 (1970).
[9] W. Helfrich, Z. Naturforsch. C **28**, 693 (1973).
[10] E. A. Evans, Biophys. J. **14**, 923 (1974).
[11] G. Monge, *Application de l'analyse à la géométrie* (Bernard, 1807).
[12] L. G. Leal, *Advanced Transport Phenomena: Fluid Mechanics and Convective Transport Processes*, Cambridge Series in Chemical Engineering (Cambridge University Press, 2007).
[13] H. Turlier and T. Betz, "Fluctuations in active membranes," in *Physics of Biological Membranes*, edited by P. Bassereau and P. Sens (Springer International Publishing, Cham, 2018) pp. 581–619.
[14] W. Yan and J. F. Brady, J. Fluid Mech. **785**, R1 (2015).
[15] N. Nikola, A. P. Solon, Y. Kafri, M. Kardar, J. Tailleur, and R. Voituriez, Phys. Rev. Lett. **117**, 098001 (2016).